# Modeling Macro-and Microstructures of Gas-Metal-Arc Welded HSLA-100 Steel

Z. YANG and T. DEBROY

Fluid flow and heat transfer during gas-metal-arc welding (GMAW) of HSLA-100 steel were studied using a transient, three-dimensional, turbulent heat transfer and fluid flow model. The temperature and velocity fields, cooling rates, and shape and size of the fusion and heat-affected zones (HAZs) were calculated. A continuous-cooling-transformation (CCT) diagram was computed to aid in the understanding of the observed weld metal microstructure. The computed results demonstrate that the dissipation of heat and momentum in the weld pool is significantly aided by turbulence, thus suggesting that previous modeling results based on laminar flow need to be re-examined. A comparison of the calculated fusion and HAZ geometries with their corresponding measured values showed good agreement. Furthermore, "finger" penetration, a unique geometric characteristic of gas-metal-arc weld pools, could be satisfactorily predicted from the model. The ability to predict these geometric variables and the agreement between the calculated and the measured cooling rates indicate the appropriateness of using a turbulence model for accurate calculations. The microstructure of the weld metal consisted mainly of acicular ferrite with small amounts of bainite. At high heat inputs, small amounts of allotriomorphic and Widmanstatten ferrite were also observed. The observed microstructures are consistent with those expected from the computed CCT diagram and the cooling rates. The results presented here demonstrate significant promise for understanding both macro-and microstructures of steel welds from the combination of the fundamental principles from both transport phenomena and phase transformation theory.

## I. INTRODUCTION

THE HSLA-100 steel has a good combination of strength, toughness, and weldability. During the gas-metal-arc welding (GMAW) of this steel, control of the geometry and microstructure is important in achieving defect-free, structurally sound, and reliable welds. Although several investigations have been undertaken on the welding of HSLA-100 steel in the past decade,[1–4] most of these studies have focused on the microstructural characterization of the weldment. In contrast, very little effort has been made to understand the evolution of weld metal macro-and microstructures from fundamental theories.

During fusion welding, the interaction of the heat source and the material leads to rapid heating, melting, and vigorous circulation of the molten metal in the weld pool. The circulation helps to transport heat in the entire weld pool. As the heat source moves away from the molten region, solidification and subsequently a series of solid-state phase transformations occur. The heat transfer and fluid flow in the weld pool affects its shape and size, cooling rate, and the resulting microstructure. An accurate knowledge of the thermal cycle in the weld metal is a prerequisite for understanding its microstructure. The direct measurement of temperature profiles in the weld pool is difficult, and noncontact techniques for measuring weld pool surface temperatures are still evolving. Measurement of cooling rates in the interior of the weld pool remains both an exciting opportunity and a formidable challenge in welding research. Mathematical modeling provides a recourse to address this problem.

In recent years, calculations of fluid flow and heat transfer in the weld pool have provided detailed insight about the welding processes that could not have otherwise been obtained.[5–19] Significant progress has been made in understanding the development of weld pool shape and size,[6–12] cooling rate,[13,14] and concentration of volatile alloying elements from the weld pool.[15,16,17] Fairly recently, efforts have been made to use these calculations to advance our understanding of the development of weld metal microstructures[18,19] and inclusion characteristics.[20] The methodologies of heat transfer and fluid flow calculations are now well accepted, and reliable commercial computer programs for the solution of the equations of conservation of mass, energy, and momentum are now generally available to achieve high efficiency and accuracy of the numerical scheme.

Previous experimental observations[21] and theoretical calculations[22,23] in gas-tungsten-arc (GTA) welding have indicated that, in many cases, the fluid flow in the weld pool is turbulent in nature. In GMAW, the high level of agitation[5] in the weld pool is aided not only by large mean velocities in a relatively small weld pool, but also by the impact of metal droplets. An effective simulation of the high rates of heat and momentum transport requires enhanced values of thermal conductivity and viscosity that are higher than their corresponding molecular values. An appropriate turbulence model is needed to calculate the enhanced values of thermal conductivity and viscosity in the weld pool. In GMAW, hot metal drops carry a significant amount of thermal and kinetic energy into the weld pool. The resulting weld pool is fairly deep at its root and its geometry exhibits a characteristic "finger penetration" pattern. Previous work has shown that

Z. YANG, Graduate Student, and T. DEBROY, Professor, are with the Department of Materials Science and Engineering, The Pennsylvania State University, University Park, PA 16802.

Manuscript submitted May 15, 1998.

**Table I. Welding Process Parameters for HSLA-100 Steel GMAW, current: 405 A, voltage: 31.3 V**

| Weld Number | Welding Velocity (mm/s) | Heat Input (kJ/mm) | Preheat (K) |
|---|---|---|---|
| 1 | 3.22 | 3.94 | 299 |
| 2 | 4.02 | 3.15 | 299 |
| 3 | 5.29 | 2.40 | 296 |

the sensible heat of the metal droplets is important in the simulation of the finger penetration pattern. However, a realistic simulation of heat transfer and fluid flow in the gas-metal-arc weld pool has not been undertaken so far.

The objective of this work is to understand the macro- and microstructures of gas-metal arc welded HSLA-100 steel from the fundamentals of the transport phenomena and phase transformation theory. A three-dimensional, transient, turbulent heat transfer and fluid flow model has been developed to predict both the weld geometry and thermal cycles. The widely used $K$-$\varepsilon$ model was adopted to simulate turbulent flow and heat transfer in the weld pool. In view of the complexities of the gas-metal-arc process, concomitant experimental work was undertaken to test the computed results. The computed shape and size of the weld pool and the heat-affected zone (HAZ) and the cooling rates were compared with corresponding experimental values. Based on classical nucleation theory, the temperature-time-transformation (TTT) diagram was calculated using an available phase transformation model,[24,25] and the diagram was used to construct a continuous-cooling-transformation (CCT) diagram. The CCT diagram and the calculated cooling rates were then used to understand the experimentally determined weld metal microstructure.

Modeling of weldment geometry and structure reported in this article represents a contribution to an expanding quantitative knowledge base in welding. Significant expansion of this knowledge base is necessary for gaining wider acceptability of welding as a mainstream, quantitative, engineering science.

## II. EXPERIMENTAL PROCEDURES

Bead-on-plate welds were deposited using GMAW with 95 pct argon-5 pct carbon dioxide shielding gas at a flow rate of 50 cubic feet per hour. Welds were made on 2-in.-thick HSLA-100 steel plates at 405 A and 31.3 V. Different cooling rates were obtained by changing the welding velocity and keeping the other variables constant. The temperature of weld metal measured by a chromel-alumel thermocouple, which was plunged into the trail of the solidifying weld pool. The cooling rates were determined from the slope of the temperature *vs* time plots. The chemical compositions of the weld metals were analyzed by a spectrometric method with the exception of oxygen, nitrogen, and hydrogen, which were determined by vacuum fusion analysis. The specimens for microstructure examination were initially etched with a 4 pct aqueous picric acid solution, followed by a Nital solution (2.5 pct nitric acid dissolved in amyl alchohol). The welding parameters and weld metal chemical composition of the HSLA-100 steel are shown in Tables I and II, respectively.

**Table II. Weld Bead Compositions of HSLA-100 Steel (in Weight Percent)**

| Weld Number | 1 | 2 | 3 |
|---|---|---|---|
| C | 0.045 | 0.050 | 0.039 |
| Mn | 1.07 | 1.07 | 1.09 |
| Si | 0.21 | 0.20 | 0.20 |
| Ni | 2.36 | 2.28 | 2.31 |
| Mo | 0.22 | 0.24 | 0.24 |
| Cr | 0.069 | 0.063 | 0.068 |
| Cu | 0.69 | 0.79 | 0.72 |
| Al | 0.015 | 0.019 | 0.017 |
| Ti | 0.013 | 0.011 | 0.010 |
| V | 0.001 | 0.001 | 0.001 |
| Nb | 0.019 | 0.020 | 0.016 |
| B | 0.0010 | 0.0016 | <0.0005 |
| O | 0.032 | 0.031 | 0.025 |
| N | 0.015 | 0.018 | 0.012 |
| P | <0.004 | 0.006 | 0.008 |
| S | 0.001 | 0.002 | <0.001 |
| H (ppm) | 1.0 | 1.1 | 1.1 |

## III. MATHEMATICAL MODELING

### A. *Fluid Flow and Heat Transfer Calculation*

The heat transfer and fluid flow were calculated by numerical solution of the equations of conservation of mass, momentum, and energy in three-dimensional form. In this work, the transient problem was transformed into a steady-state problem by solving in a coordinate system which moves with the heat source. In the moving coordinate system, the velocity and enthalpy fields are independent of time. As a consequence, the time required for computation is reduced significantly. The velocity transformation used and the transformed continuity, momentum, and energy equations can be expressed as follows.[7]

$$V = \overline{V} + V_s \qquad [1]$$

$$\nabla \cdot V = 0 \qquad [2]$$

$$\rho\nabla \cdot (\overline{V}\overline{V}) = -\nabla P + \mu_{\text{eff}}\nabla \cdot (\nabla\overline{V}) + (S_v - \rho\nabla \cdot (V_s\overline{V})) \qquad [3]$$

$$\rho\nabla \cdot (\overline{V}H) = \nabla \cdot \left(\frac{k_{\text{eff}}}{C_p}\nabla H\right) + S_1 + S_h - \rho\nabla \cdot (V_sH) \qquad [4]$$

where $V$, $\overline{V}$, and $V_s$ are the velocity at any point, convective component of the velocity, and the welding velocity, respectively; $\rho$ is the density; $P$ is the effective pressure: $C_P$ is the specific heat; $S_V$ is the source term that takes into account the combined effect of buoyancy force, Marangoni stress, and electromagnetic force; $H$ is the enthalpy; $S_h$ is the source term that takes into account the heat input from the welding source and the convective and radiative heat loss; and $S_l$ is the source term that accounts for latent heat of melting and convective transport of latent heat; $\mu_{\text{eff}}$ is the effective viscosity, and $k_{\text{eff}}$ is the effective thermal conductivity.

The governing equations were represented by a set of finite difference equations and solved iteratively on a line by line basis using a tri-diagonal matrix algorithm. The details of the procedure are described elsewhere.[26] A 52 $\times$ 34 $\times$ 30 grid system was used in the calculations. Spatially nonuniform grids were used for maximum resolution of variables. The data used for the calculation of the fluid flow and heat transfer are presented in Table III.

**Table III. Data Used for the Calculation of Velocity and Temperature Fields**

| Physical Property | value |
|---|---|
| Liquidus temperature (K) | 1782.0 |
| Solidus temperature (K) | 1742.0 |
| Density of liquid metal (kg/m$^3$) | 7200.0 |
| Viscosity of liquid (kg/m·s) | $6.0 \times 10^{-3}$ |
| Thermal conductivity of solid (J/m·s·K) | 27.1 |
| Thermal conductivity of liquid (J/m·s·K) | 83.6 |
| Specific heat of solid (J/kg·K) | 702.0 |
| Specific heat of liquid (J/kg·K) | 806.7 |
| Latent heat of melting (J/kg) | $267.6 \times 10^3$ |
| Temperature coefficient of surface tension (N/m·K) | $-0.43 \times 10^{-3}$ |

After the solution of the transformed momentum and energy equations, a steady-state temperature field can be obtained. At any given location ($x$, $y$, $z$), the variation of temperature with time can be expressed as

$$T(x, y, z, t_2) = \frac{Ts(\xi_2, y, z) - Ts(\xi_1, y, z)}{\xi_2 - \xi_1} V_s(t_2 - t_1) + T(x, y, z, t_1) \quad [5]$$

where $T_s(\xi_2, y, z)$ and $T_s(\xi_1, y, z)$ are the steady-state temperatures at coordinates ($\xi_2$, $y$, $z$) and ($\xi_1$, $y$, $z$), respectively; $\xi_2 - \xi_1$ is the distance traveled by the arc in time ($t_2 - t_1$); $V_s$ is the welding velocity; and $T(x, y, z, t_2)$ and $T(x, y, z, t_1)$ are the temperatures at times $t_1$ and $t_2$, respectively.

1. *Turbulent fluid flow and heat transfer calculation by the K-ε model*

An important component in the present model is the incorporation of the $K$-$\varepsilon$ model to calculate the turbulent fluid flow and heat transfer in the weld pool under the present welding conditions. A detailed description of the $K$-$\varepsilon$ model was given by Launder and Spalding.[27] Only the salient features of the model are presented here.

The effects of turbulence on the fluid flow and heat transfer were included through the use of effective viscosity and thermal conductivity. The effective viscosity and thermal conductivity can be expressed as

$$\mu_{\text{eff}} = \mu_t + \mu \quad [6]$$

$$k_{\text{eff}} = \mathrm{k}_t + k \quad [7]$$

where $\mu_{\text{eff}}$ and $k_{\text{eff}}$ are effective viscosity and thermal conductivity, $\mu_t$ and $K_t$ are the turbulence values, and $\mu$ and $k$ are the molecular values. Unlike the molecular viscosity and thermal conductivity, which are physical properties, the turbulent viscosity and thermal conductivity are the properties of both the fluid and the flow system. The turbulent viscosity is calculated by

$$\mu_t = \frac{C_\mu \rho K^2}{\varepsilon} \quad [8]$$

where $C_\mu$ is an empirical constant, $K$ is the turbulent kinetic energy, and $\varepsilon$ is the dissipation rate of the turbulent kinetic energy. The value of turbulent viscosity can be determined through solution of the equations of conservation of $K$ and $\varepsilon$ as follows:

$$\rho \frac{DK}{Dt} = \frac{1}{\sigma_k}\left\{\frac{\partial}{\partial x}\left[\mu_t \frac{\partial K}{\partial x}\right] + \frac{\partial}{\partial y}\left[\mu_t \frac{\partial K}{\partial y}\right] + \frac{\partial}{\partial z}\left[\mu_t \frac{\partial K}{\partial z}\right]\right\} + \mu_t G_k - \varepsilon \quad [9]$$

$$\rho \frac{D\varepsilon}{Dt} = \frac{1}{\sigma_\varepsilon}\left\{\frac{\partial}{\partial x}\left[\mu_t \frac{\partial \varepsilon}{\partial x}\right] + \frac{\partial}{\partial y}\left[\mu_t \frac{\partial \varepsilon}{\partial y}\right] + \frac{\partial}{\partial z}\left[\mu_t \frac{\partial \varepsilon}{\partial z}\right]\right\} + \frac{\varepsilon}{K}(C_1 G_k - C_2 \rho \varepsilon) \quad [10]$$

where $\sigma_\kappa$, $\sigma_\varepsilon$, $C_1$, and $C_2$ are empirical constants: $\mu_t G_k$, is the turbulent counterpart to the viscous dissipation; and $G_k$ is calculated by

$$G_k = 2\left\{\left[\frac{\partial \overline{v_x}}{\partial x}\right]^2 + \left[\frac{\partial \overline{v_y}}{\partial y}\right]^2 + \left[\frac{\partial \overline{v_z}}{\partial z}\right]^2\right\} + \left\{\left[\frac{\partial \overline{v_y}}{\partial y} + \frac{\partial \overline{v_y}}{\partial x}\right]^2 + \left[\frac{\partial \overline{v_x}}{\partial z} + \frac{\partial \overline{v_z}}{\partial x}\right]^2 + \left[\frac{\partial \overline{v_y}}{\partial z} + \frac{\partial \overline{v_z}}{\partial y}\right]^2\right\} \quad [11]$$

At the vertical symmetry plane, the boundary conditions for $K$ and $\varepsilon$ are given by $\partial K/\partial y = 0$ and $\partial \varepsilon/\partial y = 0$. The turbulence kinetic energy $K$ on the free surface was assumed to be 5 pct of the mean kinetic energy in the present calculation. Similar boundary conditions are commonly used in systems where the boundary values are not known from other considerations.[28] The value of $\varepsilon$ on the free surface was determined by the following equation.[29]

$$\varepsilon = \frac{K^{3/2}}{fL} \quad [12]$$

where $f$ is a constant ($=0.3$) and $L$ is the characteristic length of the weld pool. At the solid-liquid interface, the values of $K$ and $\varepsilon$ were forced to be zero by using a very large viscosity in the solid region. The turbulent thermal conductivity is related to the turbulent viscosity by the turbulent Prandtl number, $\mathrm{Pr}_t = C_p \mu_t / k_t = 0.9$. Thus, the spatial distribution of viscosity and thermal conductivity of the liquid metal can be calculated from the solution of Eqs. [9] and [10].

2. *Simulation of the metal droplet transfer*

The difficulty encountered in the simulation of the GMAW process comes from the transfer of metal drops and the resulting heat and momentum transfer to the weld pool. The droplets are responsible for the characteristic pool shape with finger penetration. Depending on the welding conditions, the metal transfer mechanism can be roughly classified into three modes.[30] subthreshold (<200 A), globular (200 to 250 A), and streaming (>250 A). In addition to these three well-recognized modes, at very high currents (>480 A), metal transfer may take place by rotating mode.[34] The streaming mode is associated with a self-induced magnetic field, which exerts a strong radially constrictive force. This force suppresses the normal droplet mode and constricts the molten tip into a taper from which small droplets transfer at high frequency and velocity across the arc.[31] These droplets are responsible for the finger penetration in the GMAW process.[31] The overheated metal droplets deliver their

excess heat to the molten pool. This effect is more intense at high currents, because the droplets are then transported deeply into the weld pool as a result of the rapid succession of impacts.

The heat transfer from the metal droplets has been simulated by considering the existence of a cylindrical volumetric heat source in the weld pool.[32,33] A procedure to calculate the dimensions of this cylindrical volumetric heat source was suggested by Lancaster.[32] Kumar and Bhaduri[33] modified the calculation of the depth of the volumetric heat source. The dimensions of the volumetric heat source are determined by the parameters such as the drop size, shape, velocity, and frequency. The governing equations for calculating the volumetric heat source are given subsequently. The detailed derivations of these equations are available in the literature.[32] The depth of the cylindrical cavity resulting from the impact of the drops can be estimated[32] from Eq. [13].

$$h = \left( - \frac{2\gamma}{a\rho g} + \sqrt{\left[ \left( \frac{2\gamma}{a\rho g} \right)^2 + \frac{a v_d^2}{6g} \right]} \right) \qquad [13]$$

where $h$ is the estimated depth of the cavity caused by the impact of metal droplets, $\gamma$ is surface tension, $\rho$ is the density of liquid metal, $g$ is acceleration due to gravity, $a$ is the diameter of the droplet, and $v_d$ is the droplet velocity. The droplet velocity is not available for the exact welding conditions investigated in this article. The data used here were extrapolated from the reported droplet velocities[33] at relatively lower currents (232 to 300 A). The extrapolation is justified because the metal transfer under both conditions takes place by streaming mode.[30] Only when the current exceeds 480 A may the metal transfer take place by rotating mode.[34] The cavity tends to fill between the impingement of two successive droplets. An approximate means of estimating the time to fill the cavity (and hence the droplet rate required to maintain it) is to consider acceleration of a slug of liquid, equal in volume to that of the cavity, into the weld pool. The effective depth can be calculated as $h - x$, where $x$ is the distance traveled by the center of mass of the slug and calculated[31] from Eq. [14]:

$$x = \left( h + \frac{2\gamma}{a\rho h} \right) \left\{ 1 - \left| \cos \left[ \left( \frac{g}{h} \right)^{1/2} t \right] \right| \right\} \qquad [14]$$

According to Kumar and Bhaduri[33] the droplets mix completely in the weld pool below the cavity in a cylindrical region having both the radius and height equal to the diameter of drops. Thus, the effective depth of the volumetric heat source can be calculated as $h - x + a$, where $a$,is the droplet diameter. The diameter of the droplets was estimated from the following equation.[32]

$$R_d = \frac{\pi (R_d + R_e)}{1.25 n^2 \left( 1 + \dfrac{\mu_0 I^2}{\pi^2 (R_e + R_d) \gamma} \right)^{1/2}} \qquad [15]$$

where $R_d$ and $R_e$ are the radius of the droplet and electrode, respectively; $n$ is the ratio of the drop length and diameter; $\mu_0$ is the permeability of free space; $I$ is the current; and $\gamma$ is the surface tension. The data used for the calculation of the volumetric heat source and the calculated results are shown in Tables IV and V, respectively.

The total energy absorbed by the workpiece in the GMAW process consists of two parts: energy transfer from the arc and transport of sensible heat of the metal droplets. The former is the product of the voltage, current, and efficiency of the process (approximately 8873 J/s). The energy transported by the droplets was assumed to be uniformly distributed in the cylindrical cavity. Under the conditions of the present experiments, the droplets, at a temperature[35] of about 2673 K, carry an energy of 2050 kJ/kg. From the wire feed rate and the diameter of the wire, the volume of the metal droplets is estimated to be $22.5 \times 10^{-8}$ m$^3$/s corresponding to a droplet delivering rate of $1.73 \times 10^{-3}$ kg/s. Thus, the energy transported by the metal droplets is approximately 3550 J/s, which accounts for about 40 pct of the total energy absorbed by the workpiece.

**Table IV. Data Used for the Calculation of the Volumetric Heat Source**

| | |
|---|---|
| $\gamma$ surface tension | 1.2 N/m |
| $r$ density of liquid metal | 7200 kg/m$^3$ |
| $g$ acceleration of gravity | 9.8 m/s$^2$ |
| $a$ diameter of droplet | $2R_d$ |
| $v_d$ droplet velocity | 5.5 m/s |
| $R_e$ radius of electrode | $1.6 \times 10^{-3}$ m |
| $n$ ratio of the droplet length and diameter | 3.5 (estimated) |
| $\mu_0$ the permeability of free space | $1.257 \times 10^{-6}$ henry/m |
| $I$ current | 405 A |
| $t$ time interval between two successive drops | 1/840 (estimated) |

## B. *Phase Transformation Calculation*

During cooling of the weld metal, allotriomorphic ferrite is the first phase to form from the decomposition of austenite in low alloy steels. It nucleates at the austenite grain boundaries and grows by a diffusional mechanism. As the temperature decreases, diffusion becomes sluggish and displacive transformation is kinetically favored. At relatively low undercoolings, plates of Widmanstatten ferrite forms by a displacive mechanism. At further undercoolings, bainite nucleates by the same mechanism as Widmanstatten ferrite and grows in the form of sheaves of small platelets. Acicular ferrite nucleates intragranularly at inclusions and is assumed to grow by the same mechanism as bainite in the present model.[24] The morphology of acicular ferrite differs from that of conventional bainite because the former nucleates intragranularly at inclusions and within large austenite grains, while the latter nucleates initially at austenite grain boundaries and grows by the repeated formation of subunits to generate the classical sheaf morphology.

Based on the thermodynamic and kinetic theories, the TTT diagram can be calculated using an available phase transformation model,[24,25] which has been proven to be successful in modeling low alloy weld microstructures.[18,19,36,37] By using the "Scheil" additive rule,[38] the CCT diagrams can be calculated from the TTT diagram. Thus, the phase constituents in the resultant microstructure can be understood from a combination of the calculated cooling rates and CCT diagrams. The flow chart of the mathematical model is shown in Figure 1.

**Table V. The Calculated Dimensions of Cylindrical Volume Heat Source**

| Welding Parameters | | | | | | | | Volumetric Heat-Source Dimensions | |
|---|---|---|---|---|---|---|---|---|---|
| Voltage (V) | Current (A) | Wire Feed Rate (mm/s) | Wire Diameter (mm) | Drop Radius (mm) | Drop Velocity (m/s) | Drop Frequency (per sec) | *h-x* (mm) | Radius (mm) | Height (mm) |
| 31 | 405 | 112 | 1.6 | 0.4 | 5.5 | 840 | 4.6 | 0.8 | 5.4 |

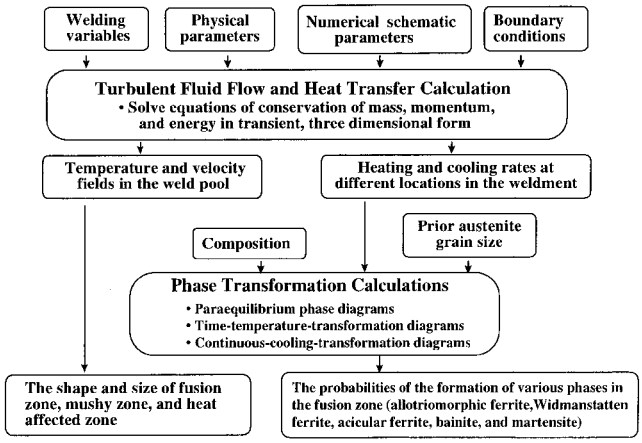


Fig. 1—Flow chart of the model.

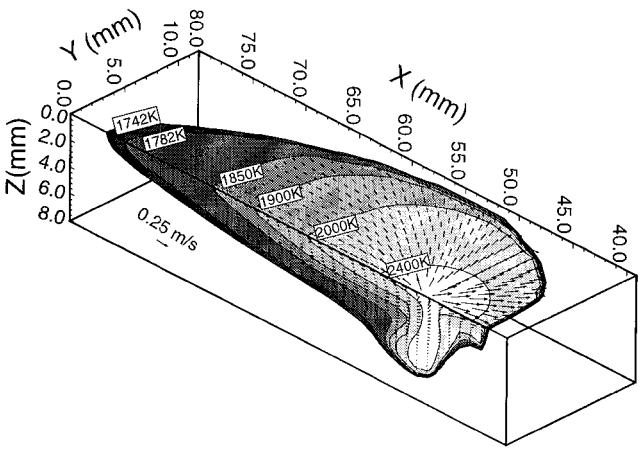


Fig. 2—Calculated temperature and velocity fields in weld 3. Welding conditions: 405 A, 31.3 V, 5.29 mm/s, and no preheat.

## IV. RESULTS AND DISCUSSIONS

### A. *Temperature and Velocity Fields*

An example of the computed temperature and velocity fields in three dimensions considering turbulent transfer of heat and momentum is shown in Figure 2. In this figure, the temperature field is indicated by contour lines and the velocity field is represented by the arrows. The general features of the calculated temperature field are consistent with the results reported in the literature.[9] In front of the heat source, the temperature gradient is greater than that behind the heat source. The high-temperature gradient results in slightly greater liquid metal velocities in front of the heat source than behind the heat source. On the surface of the weld pool, the liquid metal moves from the center to the periphery. This is expected for a metal with a very low concentration of surface active elements (*e.g.*, low sulfur and free oxygen contents), which results in a negative temperature coefficient[11] of surface tension $d\gamma/dT$. The distributions of turbulent viscosity, thermal conductivity, kinetic energy, and dissipation rate in the weld pool are shown in Figure 3. These quantities are affected by the fluid motion in the weld pool. It can be observed that the maximum values of these variables lie in the middle of the weld pool and the values decrease progressively from the center to the periphery. This is expected because the circulation of the molten metal is most intense near the surface and the level of turbulence decreases progressively as the fluid approaches the solid surface. A very thin layer called a "laminar sublayer" exists near the solid surface, in which the role of turbulence is negligible and the laminar flow dominates. The maximum dimensionless viscosity ($\mu_t/\mu$) and thermal conductivity ($k_t/k$) values were found to be 18 and 4.5, respectively. The calculated dimensionless viscosity ($\mu_t/\mu$) and thermal conductivity ($k_t/k$) values and their spatial distribution patterns are comparable with those reported in the literature.[22,23] The high values of these ratios indicate that the dissipations of heat and momentum in the weld pool are significantly aided by turbulence. In most previous research on the simulation of heat transfer and fluid flow in the weld pool, the viscosity and thermal conductivity values were arbitrarily enhanced by a constant factor. The computed turbulent viscosity and thermal conductivity values presented here clearly show that these quantifies vary strongly depending on the location within the weld pool. Therefore, accurate calculations of temperature and velocity fields must use an appropriate turbulence model.

### B. *Weld Geometry*

The geometry of the fusion zone, mushy zone, and HAZ can be predicted from the calculated temperature field, as shown in Figure 4. The fusion zone is determined by the liquidus temperature (1782 K). The mushy zone is the region between the liquidus and solidus temperatures, *i.e.*, 1782 and 1742 K, respectively. The geometry of the HAZ can also be determined from the eutectoid temperature ($Ae_1$), which is known[39] to be about 873 K for HSLA-100 steel. From Figure 4, it is observed that the width of the fusion zone, the depth of the finger penetration, and the shapes of both fusion zone and HAZ predicted by the model agreed well with the corresponding experimental results. As the welding velocity increases, the heat input per unit length decreases. Therefore, the depth of finger penetration and the width of fusion zone decrease as the welding velocity increases. As a consequence of the finger penetration in the

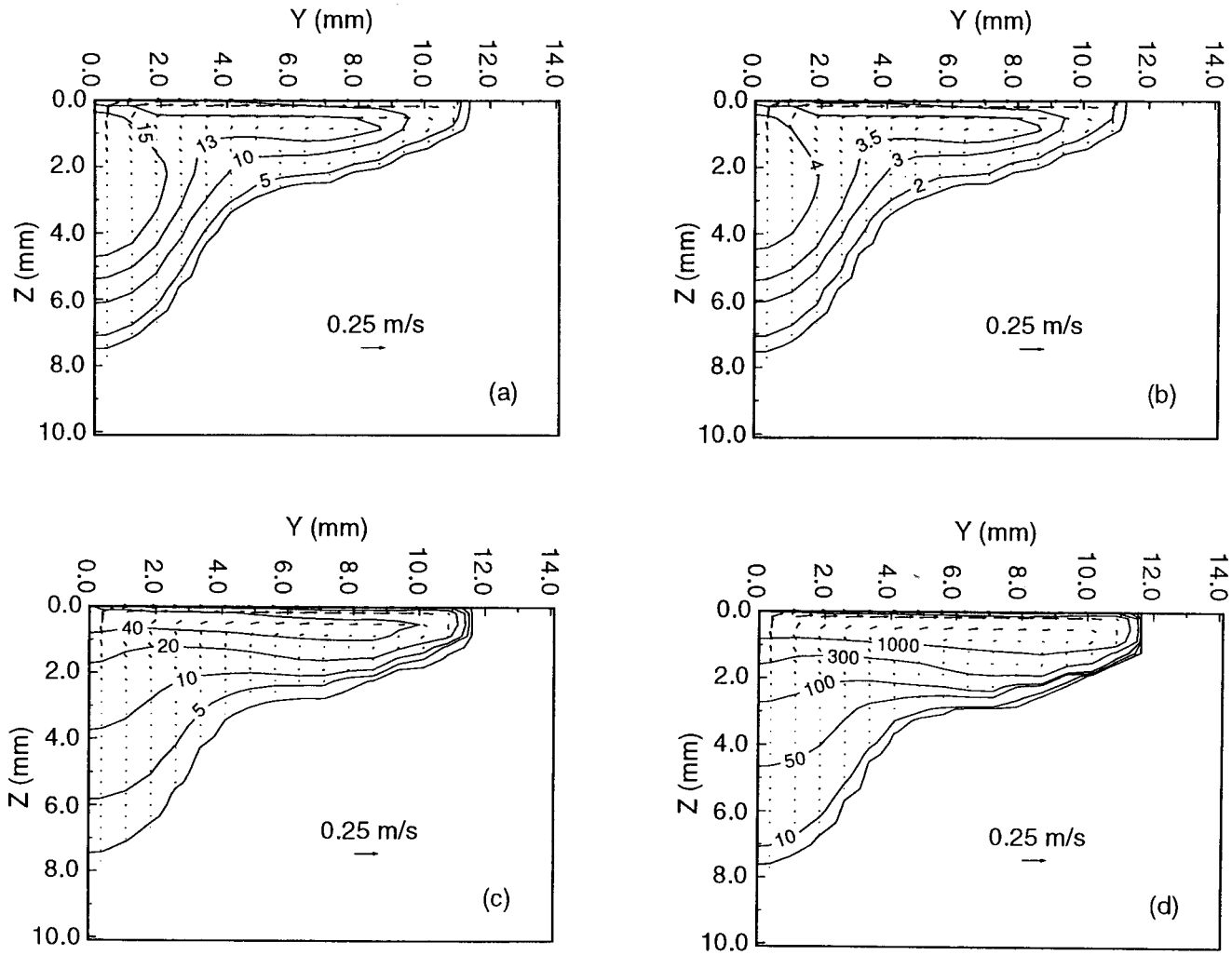


Fig. 3—Distribution of turbulent variables in the weld pool: (*a*) dimensionless viscosity, $\mu_t/\mu$ (*b*) dimensionless thermal conductivity, $k_t/k$; (*c*) turbulent kinetic energy ($m^2/s^2 \times 10^{-4}$); and (*d*) dissipation rate of turbulent kinetic energy ($m^2/s^3 \times 10^{-4}$).

fusion zone, the shape of the HAZ in the GMAW weld also exhibits certain specific features. The upper surface of the HAZ (1742 K) has the finger shape, while the lower surface of the HAZ (873 K) is rather hemispherical. Actually, the lower limit results from the Gaussian distribution of the heat source. Consequently, the thickness of the HAZ varied spatially, with the size in the middle part thicker than those in the top and bottom parts. Although the shape and size of the mushy zone can be theoretically predicted, the mushy zone cannot be identified in the micrographs in Figure 4 because of its small size and the low magnification of the micrographs.

The calculated and experimental fusion zone and the HAZ dimensions are presented in Table VI. Because the shape of the HAZ in the GMAW weld is irregular, measurements of the widths at the top ($W_T$), middle ($W_M$), and bottom ($W_B$) of the HAZ were compared with the corresponding theoretically calculated values in Table VI. The symbols $W_T$, $W_M$, and $W_B$ are defined in Figure 4. From Table VI, it is observed that the differences between the calculated and experimental sizes are small. The agreement between the calculated and experimental geometry indicates that the geometric features of the fusion zone and the HAZ in the GMAW welds can be satisfactorily calculated from the model.

### C. *Cooling Rates*

The calculated thermal cycles at different locations are shown in Figure 5. The final microstructure is determined by the cooling rate within the austenite decomposition temperature range, which is usually between 1073 and 773 K for low alloy steels. It has been proven that the cooling rate in the fusion zone is almost independent of position at temperatures well below the melting point.[15] Thus, the cooling curve at location "b" in Figure 5 was chosen, and the corresponding cooling rate between 1073 and 773 K was taken as the average cooling rate in the fusion zone. The calculated cooling rates for different welding conditions in the temperature range between 1073 and 773 K are compared with the experimental cooling curves in Figure 6. The solid and the dashed lines represent the experimental and the calculated cooling curves, respectively. The calculated average cooling rates were found to be 18.2, 22.2, and 28.6 K/s for welds 1, 2, and 3, respectively, between 1073 and 773 K. The computed times necessary for cooling from 1073 to 773 K were found to be 16.5, 13.5, and 10.5 seconds for welds 1, 2, and 3, respectively. The corresponding experimental values for welds 1, 2, and 3 were found to be 16.3, 12.8, and 10.1 seconds, respectively. Thus, the calculated

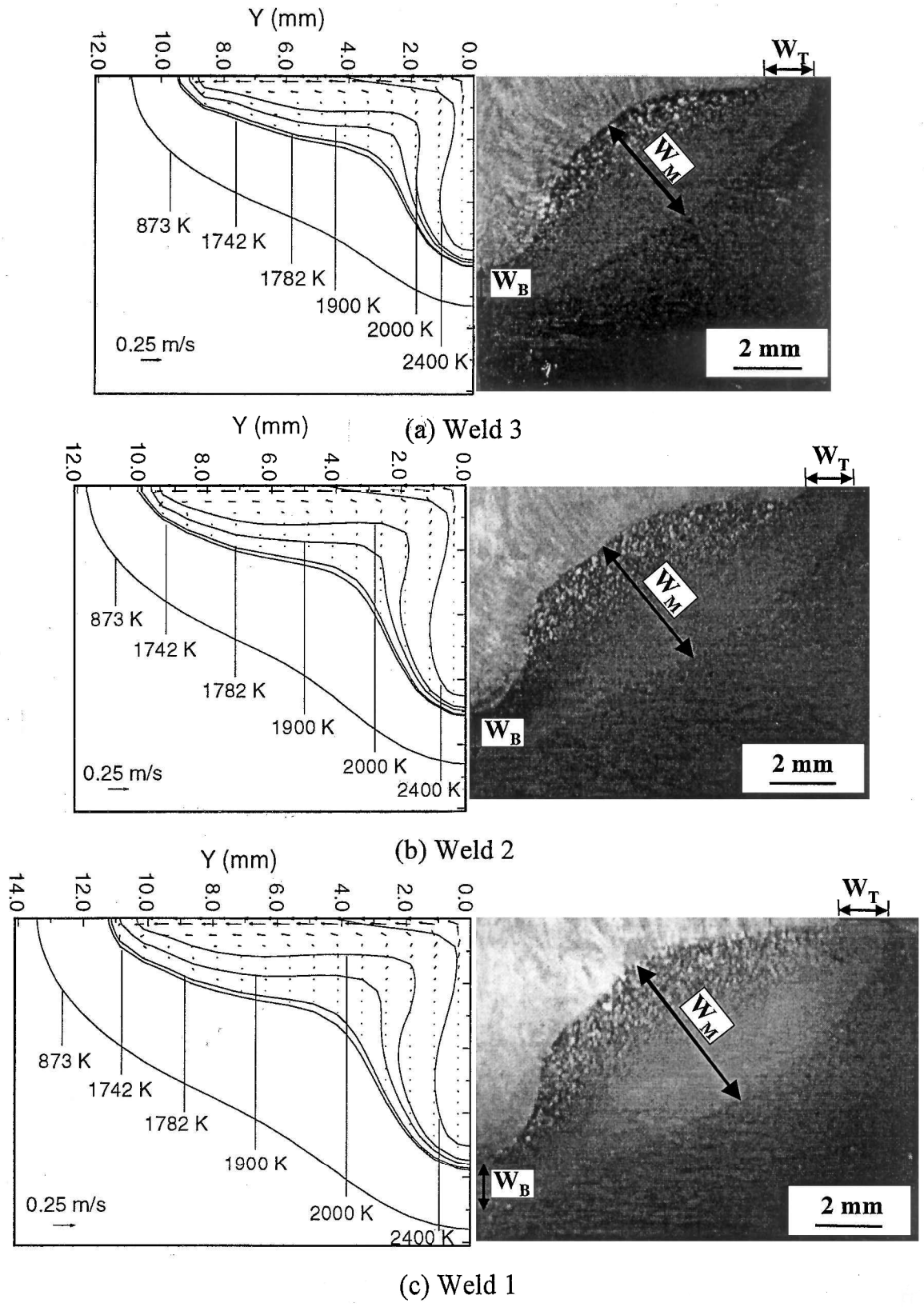


Fig. 4—Comparison of the calculated and experimental geometry of the fusion zone and the HAZ. The three welds are defined in Table 1. The heat input per unit length for the three welds is: (*a*) weld 3:2.4 kJ/mm, (*b*) weld 2:3.15 kJ/mm, and (*c*) weld 1:3.94 kJ/mm. The symbols $W_T$, $W_M$, and $W_B$ are the widths at the top, middle, and bottom of the HAZ.

**Table VI. Comparison of the Calculated and Experimental Fusion Zone and HAZ Dimensions**

| Zone | Weld Number | Dimension* | Experimental Results (mm) | Calculated Results (mm) |
|---|---|---|---|---|
| FZ | weld 1 | width | 21.8 ± 1.2 | 23.0 |
| | | depth | 7.3 ± 1.6 | 7.8 |
| | weld 2 | width | 20.8 ± 1.4 | 21.9 |
| | | depth | 7.0 ± 1.1 | 7.2 |
| | weld 3 | width | 18.0 ± 1.3 | 19.1 |
| | | depth | 6.0 ± 1.1 | 6.3 |
| HAZ | | $W_T$ | 1.8 ± 0.3 | 2.1 |
| | weld 1 | $W_M$ | 4.7 ± 0.4 | 4.0 |
| | | $W_B$ | 1.6 ± 0.2 | 1.8 |
| | | $W_T$ | 1.6 ± 0.2 | 1.7 |
| | weld 2 | $W_M$ | 4.0 ± 0.3 | 3.4 |
| | | $W_B$ | 1.4 ± 0.1 | 1.5 |
| | | $W_T$ | 1.5 ± 0.2 | 1.5 |
| | weld 3 | $W_M$ | 3.5 ± 0.3 | 3.0 |
| | | $W_B$ | 1.1 ± 0.1 | 1.2 |

*$W_T$, $W_M$, and $W_B$ are the widths at the top, middle, and bottom of the HAZ, as indicated in Fig. 4.

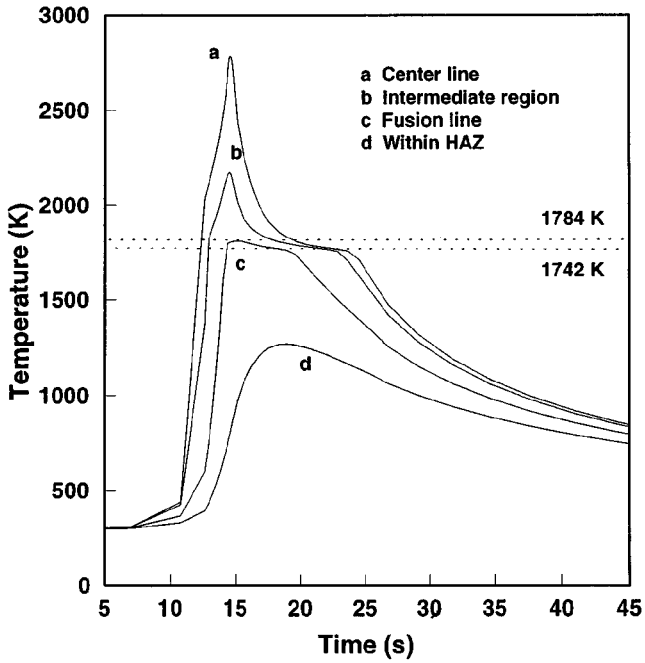


Fig. 5—Thermal cycles at different locations in weld 1.

cooling times agreed well with the experimental results. Because the cooling rates serve as a basis for understanding the fusion zone microstructures, it is important to have accurate values of cooling rates.

### D. *Microstructures*

The three weld metal microstructures obtained at different cooling rates are shown in Figure 7. Lenticular acicular ferrite was found to be the dominant phase in all these welds. Due to different cooling rates, microstructural differences among the three welds can also be observed in Figure 8. At relatively higher heat input, small amounts of allotriomorphic and Widmanstatten ferrites were observed to form at some of the prior austenite grain boundaries in welds 1 and 2. However, these ferrites were not observed in weld 3, which was produced under relatively lower heat input. Some amount of bainite in the form of sheaves was observed to form at prior austenite grain boundaries in the three welds, as shown in Figure 8(c).

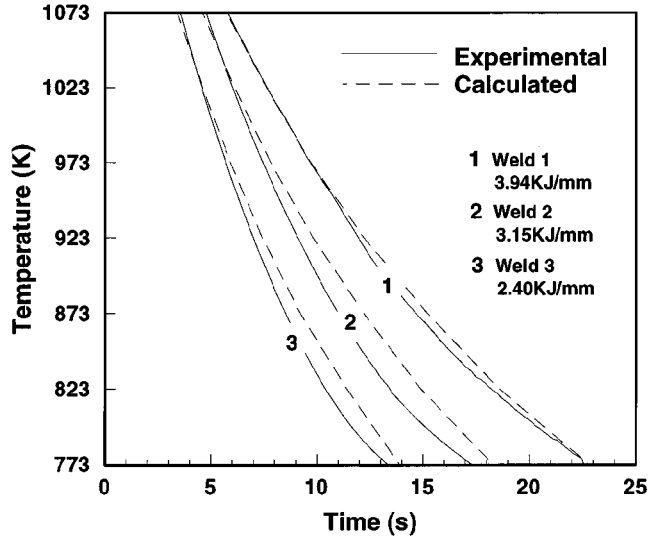


Fig. 6—Comparison of the experimental and calculated cooling rates.

The computed TTT diagram for the three welds with similar chemical compositions is shown in Figure 9. The upper *C* curve represents the time taken for initiation of the allotriomorphic ferrite formation by diffusional mechanism. The lower *C* curve represents the Widmanstatten ferrite, acicular ferrite, and bainite, all of which are assumed to form by displacive mechanism. Because the first solidified regions are depleted of solutes and these regions are first transformed to ferrite during austenite decomposition, the computed equilibrium concentrations of the solute-depleted regions are shown in Table VII. The corresponding TTT diagram in the solute-depleted regions was shown as dashed lines in Figure 9. To understand the effect of the cooling rate on the microstructure, the computed TTT diagram was transformed to a CCT diagram and the cooling curves were imposed on this CCT diagram, as shown in Figure 10. It was found that the cooling curves for all the welds intercepted with the displacive curve. Thus, acicular ferrite and bainite were expected to form in all three welds. Because the diffusional curve had only interceptions with the cooling curves of welds 1 and 2 and not with the cooling curve of weld 3, allotriomorphic ferrite was expected to form in welds 1 and 2 but not in weld 3. Thus, the observed microstructure is consistent with the computed cooling rates and CCT diagram.

## V. SUMMARY AND CONCLUSIONS

1. A comprehensive turbulent fluid flow and heat transfer model was developed to simulate the temperature and velocity fields in three dimensions, the cooling rates, and the shape and size of the fusion zone and HAZ. The high computed values of turbulent viscosity and thermal conductivity indicated that the transport of heat and momentum in the weld pool was significantly aided by turbulence.

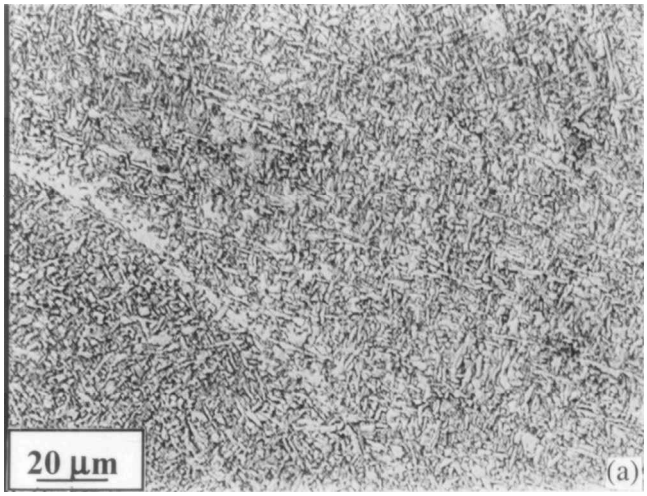


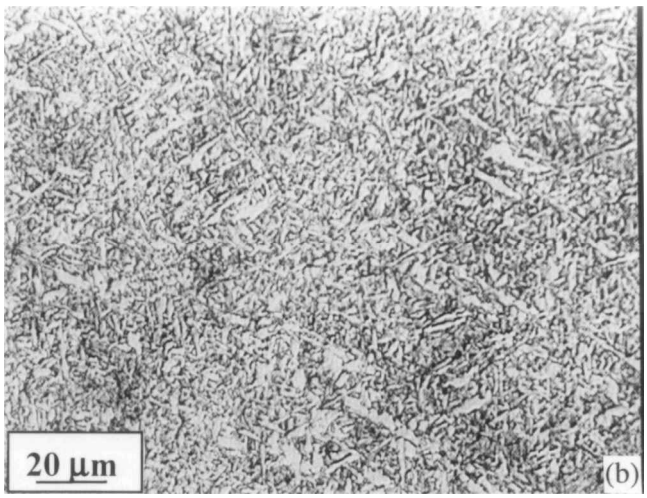


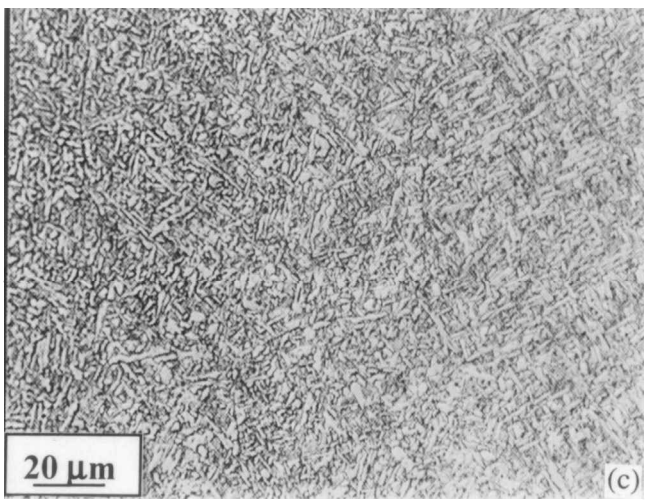


Fig. 7—(*a*) through (*c*) Optical microstructure in the fusion zone. Magnification 500 times.

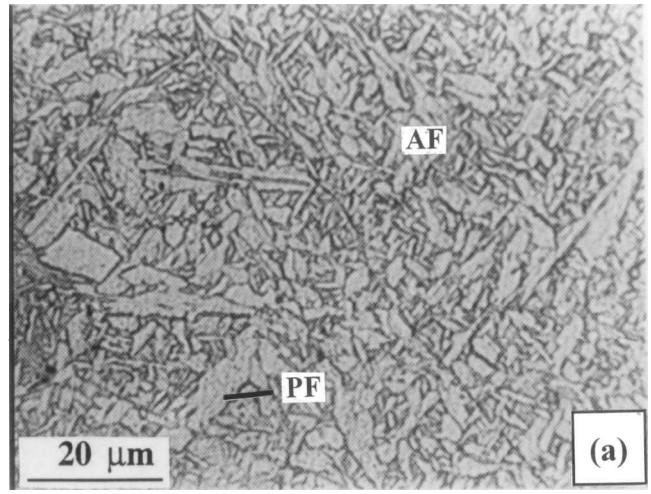


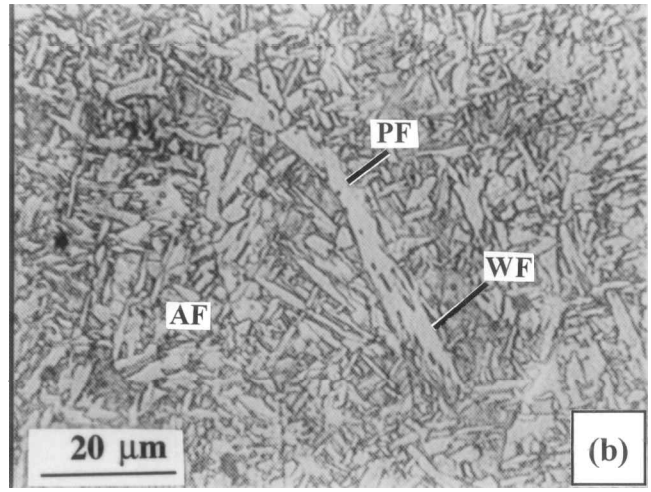


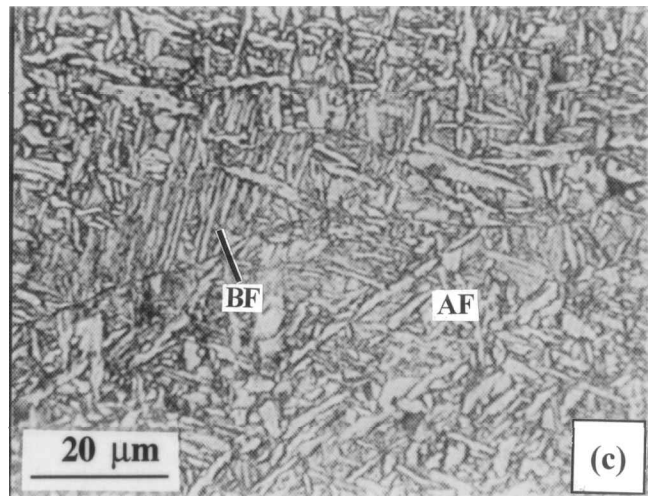


Fig. 8—Optical microstructures in some local regions of the fusion zone. Magnification 1000 times: (*a*) weld 1, (*b*) weld 2, and (*c*) weld 3. The symbols PF, WF, AF, and BF represent allotriomorphic, Widmanstatten, acicular, and bainitic ferrites, respectively.

2. Finger penetration, which is a unique feature of the fusion zone geometry of the GTA welded steel, could be satisfactorily predicted by the model. Fair agreement was achieved between the calculated shape and size of the fusion zone and the HAZ and the corresponding experimentally observed values.

3. The calculated cooling rates agreed fairly well with the experimental results. The calculated cooling rates coupled with a computed CCT diagram were used to understand the microstructures in the fusion zone.

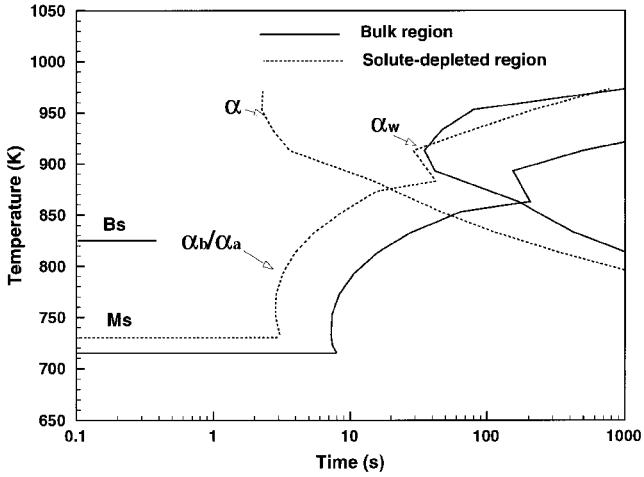


Fig. 9—Calculated TTT diagrams for weld 1 from compositions in bulk region and solute-depleted region. The symbols $\alpha$, $\alpha_w$, $\alpha_a$, and $\alpha_b$ represent allotriomorphic, Widmanstatten, acicular, and bainitic ferrites, respectively.

**Table VII. The Calculated Equilibrium Concentrations in Solute-Depleted Regions (Weight Percent)**

| Weld Number | C | Mn | Si | Ni | Mo | Cr | V |
|---|---|---|---|---|---|---|---|
| 1 | 0.045 | 0.80 | 0.16 | 1.09 | 0.11 | 0.057 | 0.0007 |
| 2 | 0.050 | 0.80 | 0.15 | 1.05 | 0.12 | 0.052 | 0.0007 |
| 3 | 0.039 | 0.82 | 0.15 | 1.11 | 0.12 | 0.056 | 0.0007 |

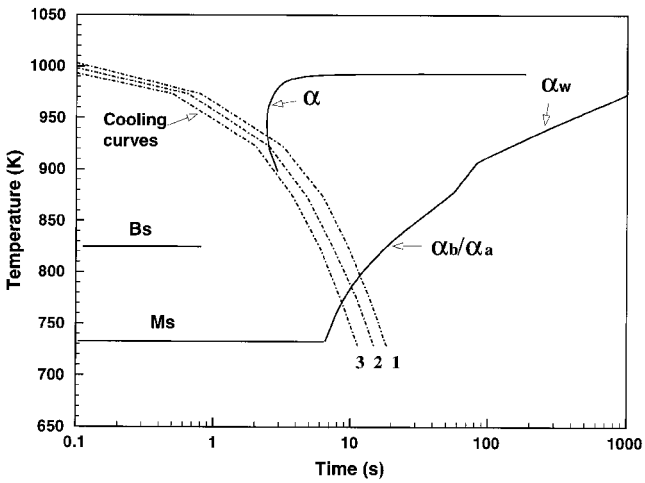


Fig. 10—Calculated CCT diagrams of weld 1 from composition in the solute-depleted region. The symbols $\alpha$, $\alpha_w$, $\alpha_a$, and $\alpha_b$ represent allotriomorphic, Widmanstatten, acicular, and bainitic ferrites, respectively. $M_s$ and $B_s$ are the starting temperatures for martensite and bainite formation, respectively.

4. The weld metal microstructures in the HSLA-100 steel consisted predominantly of acicular ferrite with small amounts of bainite. Small amounts of allotriomorphic and Widmanstatten ferrites were also observed at high heat inputs. The observed microstructures are consistent with those expected from the computed CCT diagram and the cooling rates.


## ACKNOWLEDGMENTS

This research was supported by a grant from the United States Department of Energy, Office of Basic Energy Sciences, Division of Materials Sciences. The authors thank Dr. S.A. David, Dr. S.S. Babu, and Mr. G.L. Franke for helpful discussions. The authors are grateful to Dr. H.K.D.H. Bhadeshia for help with the microstructure calculations.


## NOMENCLATURE

| | |
|---|---|
| $a$ | diameter of metal droplet (m) |
| $C_1$, $C_2$, $C_\mu$ | empirical constants in $K \sim \varepsilon$ model |
| $C_p$ | specific heat (J/kg·K) |
| $f$ | constant in Eq. [12] |
| $g$ | acceleration of gravity, (m/s$^2$) |
| $G_K$ | Cartesian tensor notation in $K \sim \varepsilon$ model (s$^{-2}$) |
| $h$ | estimated depth of the cavity caused by the impact of droplet (m) |
| $H$ | enthalpy (J/kg) |
| $I$ | current (A) |
| $k$ | molecular value of thermal conductivity (J/m·s·K) |
| $k_{\text{eff}}$ | effective thermal conductivity (J/m·s·K) |
| $k_t$ | turbulent thermal conductivity (J/m·s·K) |
| $K$ | turbulent kinetic energy (m$^2$/s$^2$) |
| $n$ | ratio of the droplet length and diameter |
| $P$ | effective pressure (N/m$^2$) |
| $\text{Pr}_t$ | turbulent Prandtl number |
| $R_d$ | radius of droplet (m) |
| $R_e$ | radius of electrode (m) |
| $S_h$ | heat source term considering heat input from welding source and heat loss by convection and radiation (J/s·m$^2$) |
| $S_l$ | heat source term considering latent heat of melting and convective transport of latent heat (J/s·m$^2$) |
| $S_v$ | momentum source term considering the combined effect of buoyancy force, Marangoni stress, and electromagnetic force (N/m$^3$) |
| $t$ | time (s) |
| $T_s(\xi, y, z)$ | temperature at coordinate ($\xi$, $y$, $z$ in steady-state temperature field (K) |
| $T(x, y, z, t)$ | temperature at coordinate ($x$, $y$, $z$) at time $t$ (K) |
| $v_d$ | droplet velocity (m/s) |
| $\overline{v}_x$, $\overline{v}_y$, $\overline{v}_z$ | velocity components in the $x$, $y$, and $z$ directions, respectively (m/s) |
| $V$ | transformed velocity (m/s) |
| $\overline{V}$ | convective component of the velocity (m/s) |
| $V_s$ | welding velocity (m/s) |
| $x$ | distance traveled by the center of mass of the slug (m) |
| $\gamma$ | surface tension (N/m) |
| $\varepsilon$ | dissipation rate of turbulent kinetic energy (m$^2$/s$^3$) |
| $\xi_1$, $\xi_2$ | coordinates in $x$ direction at time $t_1$ and $t_2$, respectively (m) |
| $\mu$ | molecular value of viscosity (kg/m·s) |
| $\mu_{\text{eff}}$ | effective viscosity (kg/m·s) |
| $\mu_t$ | turbulent viscosity (kg/m·s) |
| $\mu_0$ | permeability of free space (henry/m) |

| | |
|---|---|
| $\rho$ | density (kg/m$^3$) |
| $\sigma_k$, $\sigma_\varepsilon$ | empirical constants in $K \sim \varepsilon$ model |

## REFERENCES


1. J.M.B. Losz and K.D. Challenger: *Recent Trends in Welding Science and Technology*, S.A. David and J.M. Vitek, eds., ASM INTERNATIONAL, Materials Park, OH, 1990, pp. 229-35.
2. D.G. Howden, L. Zhang, R.S. Green, K. Smapath, J.H. Devletian, and D. Singh: *International Trends in Welding Science and Technology*, S.A. David and J.M. Vitek, eds, ASM INTERNATIONAL, Materials Park, OH, 1993, pp. 359-64.
3. R.P. Martukanitz, P.R. Howell, and W.A. Pratt: *International Trends in Welding Science and Technology*, S.A. David and J.M. Vitek, eds., ASM INTERNATIONAL, Materials Park, OH, 1993, pp. 271-79.
4. R.W. Fonda, G. Spanos, and R.A. Vandermeer: in *Trends in Welding Research*, H.B. Smartt, J.A. Johnson, and S.A. David, eds., ASM INTERNATIONAL, Materials Park, OH, 1996, pp. 277-82.
5. H. Davis: Ph.D. Thesis, University of Adelaide, Adelaide, Australia, September, 1995.
6. W. Pitscheneder, T. DebRoy, K. Mundra, and R. Ebner: *Weld. J.*, 1996, vol. 75 (3), pp. 71s-80s.
7. K. Mundra, T. DebRoy, and K. Kelkar: *Numerical Heat Transfer*, 1996, vol. 29, pp. 115-29.
8. R.T.C. Choo, J. Szekely, and S.A. David: *Metall. Trans. B*, 1992, vol. 23B, pp. 371-84.
9. S. Kou and Y.H. Wang: *Metall. Trans. A*, 1986, vol. 17A, pp. 2265-70.
10. C. Chan, J. Mazumder, and M.M. Chen: *Metall. Trans. A*, 1984, vol. 15A, pp. 2175-84.
11. T. DebRoy and S.A. David: *Rev. Modern Phys.*, 1995, vol. 67 (1), pp. 85-112.
12. T. Zacharia, S.A. David, J.M. Vitek, and T. DebRoy: *Weld. J.*, 1989, vol. 68 (12), pp. 499s-509s.
13. K. Mundra, T. DebRoy, T. Zacharia, and S.A. David: *Weld. J.*, 1992, vol. 71 (9), pp. 313s-320s.
14. K. Mundra, J.M. Blackburn, and T. DebRoy: *Sci. Technol. Welding Joining*, 1997, vol. 2 (4), pp. 174-84.
15. A. Block-Bolten and T.W. Eager: *Metall. Trans. B*, 1984, vol. 15B, pp. 461-69.
16. P.A.A. Khan and T. DebRoy: *Metall. Trans. B*, 1984, vol. 15B, pp. 641-44.
17. K. Mundra and T. DebRoy: *Weld. J.*, 1993, vol. 72 (1), pp. 1s-9s.
18. K. Mundra, T. DebRoy, S.S. Babu, and S.A. David: *Weld. J.*, 1997, vol. 76 (4), pp. 163s-171s.
19. Z. Yang and T. DebRoy: *Sci. Technol. Welding Joining*, 1997, vol. 2 (2), pp. 53-58.
20. T. Hong, W. Pitscheneder, and T. DebRoy: *Sci. Technol. Welding Joining*, 1998, vol. 3 (1), pp. 33-41.
21. M. Malinowski-Brodnicka, G. denOuden, and W.J.P. Vink: *Weld. J.*, 1990, vol. 69, pp. 52s-59s.
22. R.T.C. Choo and J. Szekely: *Weld. J.*, 1994, vol. 73 (2), pp. 25s-31s.
23. K. Hong, D.C. Weckman, and A.B. Strong: in *Trends in Welding Research*, H.B. Smartt, J.A. Johnson, and S.A. David, eds., ASM INTERNATIONAL, Materials Park, OH, 1996, pp. 399-404.
24. H.K.D.H. Bhadeshia: in *Mathematical Modeling of Weld Phenomena*, H. Cerjak and K.E. Easterling, eds., Institute of Materials, London, 1993, pp. 109-80.
25. H.K.D.H. Bhadeshia: *Metal Science*, 1982, vol. 16(3), pp. 159-65.
26. S.V. Patankar: *Numerical Heat Transfer and Fluid Flow*, Hemisphere Publishing Corporation, New York, NY, 1980.
27. B.E. Launder and B.D. Spalding: *Mathematical Models of Turbulence*, Academic Press, New York, NY, 1972.
28. W.M. Pun and D.B. Spalding: Heat Transfer Section Report No. HTS/76/2, Imperial College, London, 1976.
29. *ILLUSTRATIVE ADAPTATIONS of COMPACT-3D Version 3.1*, a general-purpose computer program for three-dimensional fluid flow and heat transfer, Innovative Research Inc., Minneapolis, MN, 1993, p. 14-2.
30. D.N. Shackleton and W. Lucas: *Weld. J.*, 1974, vol. 53 (12), pp. 537s-547s.
31. W.G. Essers and R. Walter: *Weld. J.*, 1981, vol. 60 (2), pp. 37s-42s.
32. J.F. Lancaster: *The Physics of Welding*, Pergamon Press, New York, NY, 1984.
33. S. Kumar and S.C. Bhaduri: *Metall. Mater. Trans. B*, 1994, vol. 25B, pp. 435-41.
34. L.A. Jones, T.W. Eagar, and J.H. Lang: *Weld. J.*, 1998, vol. 77 (4), pp. 135s-141s.
35. G.W. Tichellar, G. Jelmorini, and G.J.P.M. vander Henvel: *Droplet Temperature Measurement in Arc Welding*, IIW Document 212-411-77, International Institute of Welding, France, 1977.
36. L.-E. Svensson, B. Gretoft, and H.K.D.H. Bhadeshia: *Scand. J. Metall.*, 1986, vol. 15, pp. 97-103.
37. H.K.D.H. Bhadeshia, L.E. Svensson, and B. Gretoft: *Acta Metall.*, 1985, vol. 33, pp. 1271-83.
38. M. Takahashi and H.K.D.H. Bhadeshia: *Mater. Trans.*, 1991, vol. 32 (8), pp. 689-96.
39. A.D. Wilson, E.G. Hamburg, D.J. Colvin, S.W. Thompson, and Y. Krauss: *Proc. Microalloying 88, World Materials Congress*, ASM INTERNATIONAL, Materials Park, OH, 1988, pp. 259-75.